

Non-radiative decay of a dipole emitter close to a metallic nanoparticle: Importance of higher-order multipole contributions

Alexander Moroz*
Wave-scattering.com

ABSTRACT

The contribution of higher-order multipoles to radiative and non-radiative decay of a single dipole emitter close to a spherical metallic nanoparticle is re-examined. Taking a Ag spherical nanoparticle (AgNP) with the radius of 5 nm as an example, a significant contribution (between 50% and 101% of the total value) of higher-order multipoles to non-radiative rates is found even at the emitter distance of 5 nm from the AgNP surface. On the other hand, the higher-order multipole contribution to radiative rates is negligible. Consequently, a dipole-dipole approximation can yield only an upper bound on the apparent quantum yield. In contrast, the non-radiative rates calculated with the quasistatic Gersten and Nitzan method are found to be in much better agreement with exact electrodynamic results. Finally, the size corrected metal dielectric function is shown to decrease the non-radiative rates near the dipolar surface plasmon resonance.

PACS numbers: 33.50.-j, 33.50.Hv, 32.50.+d, 78.67.-n, 71.45.Gm, 73.22.Lp, 78.67.Bf

*<http://www.wave-scattering.com>

1 Introduction

Metallic surfaces are known to increase the local electromagnetic fields and modify both excitation and emission rates of proximate fluorophores, chromophores, and quantum dots [1, 2, 3, 4, 5, 6, 7, 8, 9, 10, 11, 12]. Especially promising is modifying fluorescence rates by means of metallic nanoparticles (MNPs) for addressing various issues of interest to biology [2, 3, 4, 5]. The MNPs can quench fluorescence as much as 100 times better than other quenchers of fluorescence, such as DABCYL, and open new perspectives in the use of hybrid materials as sensitive probes in fluorescence-based detection assays [2]. Molecular beacons comprising the MNP acceptors can detect minute amounts of oligonucleotide target sequences in a pool of random sequences and provide an improved detection of a single mismatch in a competitive hybridization assay for DNA mismatch detection [2]. The MNP acceptors can also be employed for probing changes in distances for protein interactions on DNA using a molecular ruler approach called nanometal surface energy transfer [9]. The MNPs induced decrease in lifetime of fluorophores can result in an effective increase in photostability. All that carries potential for the next generation superstructures in clinical diagnostic, DNA sequencing, genomics, and biological detection. The latter is the subject of a new field of radiative decay engineering that aims at a predetermined modification of decay rates [3, 5].

In theory, fluorophores, chromophores, and quantum dots are modeled as dipole emitters and the underlying problem is then that of a single dipole emitter in proximity to a MNP [1, 4, 6, 7, 8, 10, 11, 12]. In general, when the influence of a particle on the dipole emission is studied, the *outgoing* electromagnetic fields of a dipole emitter are expanded into the electromagnetic multipole fields centered at a origin of and *incident* on the particle [1, 6, 8, 13, 14, 15]. This transformation induces formally an infinite number of higher order multipole electromagnetic fields that can be characterized by the angular momentum numbers l and $-l \leq m \leq l$ [1, 6, 8, 13, 14, 15]. A recent publication by Carminati et al [10] suggested an approximate analytical approach to calculate the fluorescence decay rate and the radiative and non-radiative rates. The rates were determined solely as a function of the particle polarizability α . For instance, the *fluorescence decay* rates for a parallel (tangential) and perpendicular (radial) dipole orientation with respect to the particle surface have been determined as (cf. Eqs. (9) and (10) of Ref. [10])

$$\begin{aligned} \frac{\Gamma_{\parallel}}{\Gamma_0} &= 1 + \frac{3k^3}{2\pi} \operatorname{Im} \left[\alpha(\omega) \exp(2ikz) \left(\frac{1}{(kz)^6} + \frac{2}{i(kz)^5} - \frac{1}{(kz)^4} \right) \right], \\ \frac{\Gamma_{\perp}}{\Gamma_0} &= 1 + \frac{3k^3}{8\pi} \operatorname{Im} \left[\alpha(\omega) \exp(2ikz) \left(\frac{1}{(kz)^6} + \frac{2}{i(kz)^5} - \frac{3}{(kz)^4} \right. \right. \\ &\quad \left. \left. - \frac{2}{i(kz)^3} + \frac{1}{(kz)^2} \right) \right], \end{aligned} \quad (1)$$

where Γ_0 is the (radiative) decay rate in free space, z is the distance to the center of a nanoparticle and k stands for a wave vector.

As in Ref. [10], let us focus on the distance dependence of the various rates of a dipole emitter at a proximity to Ag spherical nanoparticle (AgNP) with radius of 5 nm. Two

different emission wavelengths of the dipole emitter will be considered: 354 nm and 612 nm. The dielectric constant of AgNP at the respective emission wavelengths is taken to be $\varepsilon(354 \text{ nm}) = -2.03 + 0.6i$ and $\varepsilon(612 \text{ nm}) = -15.04 + 1.02i$ [10, 16]. For the sake of simplicity it will be assumed throughout that the host medium is air. Already a first glance at the fluorescence decay rates in Figs. 1 and 2 suffices to appreciate marked differences between the rates obtained using the approximate analytical approach of Carminati et al and the exact results [1, 6, 8, 13, 14, 15]. The converged exact rates in Figs. 1 and 2 were obtained using the freely available code in CHEWFS [17] (see Appendix A for a brief description of the code) and comprise contributions of the induced multipoles with l up to $l_{max} = 50$. Note in passing that the rates labeled as “exact” in Figs. 1 and 2 of Ref. [10] are in fact those given by Eqs. (1). The latter correspond to a situation when all the induced higher order ($l > 1$) multipole contributions to the real exact decay rates but the dipole one ($l = 1$) are neglected. This is confirmed by Figs. 1 and 2, wherein the *nonconverged* calculations of the exact decay rates with a cut-off at $l = 1$ are shown to coincide with the approximate rates. Although the authors of Ref. [10] warned at one occasion that the validity of their expressions (1) requires the distance z to remain larger than a few radii of the MNP, the warning remained largely ignored. Indeed, had the warning been taken seriously, any discussion of the apparent quantum yield as in Fig. 3 of Ref. [10] should have been avoided in the dipole approximation: to address the apparent quantum yield and the question of fluorescence quenching at short distances, one is required to calculate various rates for the very forbidden distances z within a few radii of the MNP. In this work we discuss in depth the following issues:

1. The derivation of the particle polarizability α in [10] misses a dynamic depolarization term.
2. Even if both the radiation reaction correction and dynamic depolarization are included in α , there is, for the examples studied in [10], essentially no difference with regard to the corresponding rates obtained by substituting the static Rayleigh polarizability α_R in the formulas of [10].
3. For the examples studied in [10], the dipole-dipole coupling cannot describe satisfactorily the non-radiative rates even if the emitter is as far as three particle radii from the particle surface.
4. The familiar Gersten and Nitzan quasistatic theory [18] yields non-radiative rates that agree much better with the exact rates than those of Ref. [10].
5. Because the validity of expressions (1) requires the distance z to remain larger than a few radii of the nanoparticle, the dipole approximation of Ref. [10] cannot be applied to describe quenching [20, 21, 22, 23]. The dipole-dipole approximation can only yield an upper bound on the apparent quantum yield.
6. All the rates are affected by the size corrections to the metal dielectric function [24, 25, 26].

The paper is organized as follows. Sec. 2 introduces a hierarchy of approximations for the particle polarizability and studies the effect of a particular choice of the polarizability on the resulting rates. Although the results of Ref. [10] have just been shown to correspond to the *nonconverged* calculations of the exact decay rates with a cut-off at $l = 1$ (see Figs. 1 and 2), the behaviour of the radiative rates will be shown to be different from that of the non-radiative rates in that the $l = 1$ approximation to the radiative rates is essentially exact in the studied situation. The latter point is the subject of Sec. 3. The remaining points such as a comparison with the Gersten and Nitzan theory [18], the distance dependence of non-radiative rates, some points regarding the calculation of the power P_{abs} absorbed inside the particle, and the influence of the size correction to the bulk dielectric function on the rates are discussed in Sec. 4. We then conclude with Sec. 5. A brief description of the freely available codes, which were used to generate the results of this paper, is provided in Appendix A.

2 A hierarchy of approximations for the particle polarizability and corresponding rates

In Ref. [10] the particle polarizability was given by

$$\alpha_C(\omega) = \frac{\alpha_R(\omega)}{1 - i\frac{k^3}{6\pi}\alpha_R(\omega)}, \quad (2)$$

with α_R (denoted as α_0 in Ref. [10]) being the familiar static Rayleigh polarizability of a sphere,

$$\alpha_R(\omega) = 4\pi a^3 \frac{\varepsilon(\omega) - 1}{\varepsilon(\omega) + 2}, \quad (3)$$

where a and $\varepsilon(\omega)$ are the radius and the dielectric constant of the particle, respectively. The k^3 -dependent term is the familiar *radiative reaction correction* emphasized by earlier Ref. [27]. The radiative reaction correction applies to any oscillating dipole, be it an elementary molecular dipole or the dipole induced on a small (nano)particle, and results from the *Abraham-Lorentz equation* (see, e.g., Sec. 16.2 and Eqs. (16.8-9) of Ref. [29]). However, the exact polarizability for a sphere is obtained from Mie's solution as

$$\alpha_{Mie} = -i\frac{6\pi}{k^3} T_{E1}, \quad (4)$$

where T_{E1} is the electric dipole T-matrix element (the latter corresponds to the minus of the electric dipole Mie coefficients as given by Bohren and Huffman [30]). Upon introducing the size parameter $x = ka$, one finds in the long-wavelength limit [31]

$$\begin{aligned} \alpha_{Mie} &\sim \alpha_{Mie;as} = 4\pi a^3 \frac{\varepsilon - 1}{\varepsilon + 2 - (6\varepsilon - 12)\frac{x^2}{10} - i\frac{2x^3}{3}(\varepsilon - 1)} \\ &= \frac{\alpha_R(\omega)}{1 - \frac{3k^2}{20\pi a} \frac{\varepsilon - 2}{\varepsilon - 1} \alpha_R(\omega) - i\frac{k^3}{6\pi} \alpha_R(\omega)}. \end{aligned} \quad (5)$$

To this end note that each of the polarizabilities can be parametrized as

$$\alpha = \frac{\alpha_R}{1 - A_2 \frac{k^2}{4\pi a} \alpha_R - i A_3 \frac{k^3}{6\pi} \alpha_R}. \quad (6)$$

Here $A_2 = A_2(\varepsilon)$ ($A_2 \equiv 0$ for α_R and α_C) is in general a function of ε , and hence a *complex* function of frequency, whereas A_3 ($A_3 = 0$ for α_R ; $A_3 = 1$ for α_C and $\alpha_{Mie;as}$) is a *real* numerical constant. The special case $A_2 = A_3 = 1$ of the above parametrization corresponds to the approximate Meier and Wokaun polarizability α_{MW} [28, 31]. The polarizabilities α_R , α_C , α_{MW} , and $\alpha_{Mie;as}$ in this order approximate the particle polarizability α_{Mie} with an increasing precision. For instance, when α_C is compared against α_{MW} or $\alpha_{Mie;as}$, one immediately notices a missing k^2 -term in the denominator of α_C . The missing term is the so-called *dynamic depolarization* term [28, 31]. For a given constant homogeneous external field, the Meier and Wokaun polarizability α_{MW} presumes a constant internal field within the particle. In contrast to α_{MW} , $\alpha_{Mie;as}$ takes implicitly into account an order x^2 deviation from the constant internal field [31].

TABLE 1. The values of various polarizabilities $\bar{\alpha} = (\text{Re } \alpha, \text{Im } \alpha)$ of AgNP for $\lambda = 354$ nm and $\lambda = 612$ nm.

	$\lambda = 354$ nm	$\lambda = 612$ nm
$\alpha_R/(4\pi a^3)$	(1.249, 4.988)	(1.229, 0.0179)
$\alpha_C/(4\pi a^3)$	(1.244, 4.977)	(1.229, 0.0180)
$\alpha_{MW}/(4\pi a^3)$	(1.055, 5.068)	(1.233, 0.0181)
$\alpha_{Mie;as}/(4\pi a^3)$	(1.119, 5.036)	(1.231, 0.0181)
$\alpha_{Mie}/(4\pi a^3)$	(1.093, 5.042)	(1.231, 0.0181)

As shown in Ref. [31], the dynamic depolarization term can also be derived from the very same Green's function approach of Ref. [10], the fact that has eluded the authors of Ref. [10]. Without the dynamic depolarization term, the polarizability α_C does not take into account any size dependence of the dipolar localized surface plasmon resonance (LSPR) position. The size dependence is determined, up to the order of x^2 , by the following equation for the real part of $\varepsilon = \varepsilon' + i\varepsilon''$ (see Sec. 12.1.1 of Ref. [30]):

$$\varepsilon' \approx -2 - \frac{12x^2}{5}. \quad (7)$$

Although the dynamic depolarization term would cause for $a \gtrsim 40$ nm an appreciable difference of the rates obtained with $\alpha_{Mie;as}$ or α_{Mie} compared to those with α_C , with the radius of AgNP of mere 5 nm and $x < 0.09$, there is, in the present case, essentially no difference as to what polarizability is substituted into the approximate rate equations of Ref. [10]. The latter point is illustrated by Table 1 that lists the values of various polarizabilities, which have been introduced so far. Therefore, the difference in the fluorescence decay rates obtained using the approximate analytical approach of Carminati et al [10]

with regard to the exact results [1, 6, 8, 13, 14, 15] (see Figs. 1 and 2) cannot be the result of a wrong choice of polarizability.

To this end note that the implications of the unitary bound on the physical S matrix,

$$0 \leq SS^\dagger \leq 1. \quad (8)$$

Given the parametrization $S = 1 + 2iT$ of the S matrix, the unitarity bound implies for the physical T matrix and the polarizability

$$-\frac{1}{4} - |T|^2 \leq \text{Re } T \leq -|T|^2 \leq 0, \quad \frac{k^3}{6\pi} |\alpha|^2 \leq \text{Im } \alpha \leq \frac{k^3}{6\pi} |\alpha|^2 + \frac{3\pi}{2k^3}, \quad (9)$$

where the second bound follows from the first one on substituting $ik^3\alpha/(6\pi)$ for T . Because $\text{Im } \alpha_R \equiv 0$ for a real ε , the familiar static Rayleigh polarizability α_R violates the above physical bounds. The violation is reflected by the fact that $\sigma_{tot} \neq \sigma_{sca} + \sigma_{abs}$, where σ_{tot} , σ_{sca} , σ_{abs} are the total, scattering, and absorption cross-sections. Nevertheless, since σ_{tot} is in the present case dominated by σ_{abs} , one could in the present case calculate the rates with the familiar static Rayleigh polarizability α_R without ever noticing any difference with respect to the results obtained by means of α_C (see Figs. 3 to 6).

3 Radiative and non-radiative rates

The non-radiative rates are derived from the power P_{abs} absorbed inside the particle [1, 6, 10, 15]. Carminati et al [10] derived the following approximate expressions for the rates (see Eqs. (15) and (16) of Ref. [10]):

$$\begin{aligned} \frac{\Gamma_{nr;\parallel}}{\Gamma_0} &= \frac{3k^3}{2\pi} \left[\text{Im} [\alpha(\omega)] - \frac{k^3}{6\pi} |\alpha(\omega)|^2 \right] \left[\frac{1}{(kz)^6} + \frac{1}{(kz)^4} \right], \\ \frac{\Gamma_{nr;\perp}}{\Gamma_0} &= \frac{3k^3}{8\pi} \left[\text{Im} [\alpha(\omega)] - \frac{k^3}{6\pi} |\alpha(\omega)|^2 \right] \left[\frac{1}{(kz)^6} - \frac{1}{(kz)^4} + \frac{1}{(kz)^2} \right]. \end{aligned} \quad (10)$$

The respective radiative rates were then derived in Ref. [10] as a difference of the corresponding total decay rates in the short distance limit $ka < kz \ll 1$ (Eqs. (11),(12) in Ref. [10]) and the non-radiative rates (10). The resulting approximate expressions for the radiative rates were (Eqs. (17) and (18) of Ref. [10]):

$$\begin{aligned} \frac{\Gamma_{r;\parallel}}{\Gamma_0} &= 1 + \frac{k^6}{4\pi^2} |\alpha(\omega)|^2 \left[\frac{1}{(kz)^6} + \frac{1}{(kz)^4} \right] + \frac{k^3}{\pi} \text{Re} [\alpha(\omega)] \frac{1}{(kz)^3}, \\ \frac{\Gamma_{r;\perp}}{\Gamma_0} &= 1 + \frac{k^6}{16\pi^2} |\alpha(\omega)|^2 \left[\frac{1}{(kz)^6} - \frac{1}{(kz)^4} \right] - \frac{k^3}{2\pi} \text{Re} [\alpha(\omega)] \frac{1}{(kz)^3}. \end{aligned} \quad (11)$$

It can be verified that the above formulae of Ref. [10] hold irrespective which polarizability of Sec. 2 is used. A necessary and sufficient condition is to show that the power P_{abs} absorbed inside the particle remains to be given by the formula (see Eq. (13) of Ref. [10])

$$P_{abs} = \frac{\omega\varepsilon_0}{2} \left(\text{Im } \alpha - \frac{k^3}{6\pi} |\alpha|^2 \right) |\mathbf{E}_{exc}|^2. \quad (12)$$

The latter formula can easily be verified to follow from the more general expression

$$P_{abs} = \frac{\omega \varepsilon_0}{2k} \sigma_{abs} |\mathbf{E}_{exc}|^2, \quad (13)$$

where σ_{abs} is the absorption cross-section of a MNP. Indeed, provided that one factorizes the electric dipole element of the T-matrix (in the SI units) as $T_{E1} = i \frac{k^3}{6\pi} \alpha$ [cf Eq. (4)], the total (extinction), scattering, and absorption cross sections can be expressed as

$$\sigma_{tot} \approx -\frac{6\pi}{k^2} \text{Re } T_{E1} = k \text{Im } \alpha, \quad (14)$$

$$\sigma_{sca} \approx \frac{6\pi}{k^2} |T_{E1}|^2 = \frac{k^4}{6\pi} |\alpha|^2, \quad (15)$$

$$\sigma_{abs} \approx \frac{3\pi}{2k^2} (1 - |1 + 2T_{E1}|^2) = k \left(\text{Im } \alpha - \frac{k^3}{6\pi} |\alpha|^2 \right). \quad (16)$$

Consequently, upon substituting (16) into (13) one recovers the formula (12), irrespective of the choice of the polarizability of Sec. 2.

A comparison of the approximate and exact radiative rates is shown in Figs. 3 and 4. The results show clearly that all rates coalesce to a single line, irrespective if obtained in the dipole-dipole approximation with α_R , α_C , $\alpha_{Mie;as}$, or α_{Mie} , or as the exact radiative rates with a cut-off imposed at either $l = 1$ or $l = 50$. Thus the induced multipoles of the order $l \geq 2$ have in the present case hardly any effect on the radiative rates, because the exact radiative rates are very precisely approximated by taking into account solely the dipole-dipole interaction. The latter means that the conclusions of Carminati et al [10] regarding the distance dependence of the radiative decay rate are correct. The distance dependence is chiefly dominated by a z^{-3} dependence, with a z^{-6} dependence being visible at plasmon resonance. On the other hand the results are hardly surprising and appear to have been anticipated by Gersten and Nitzan, who also approximate the exact radiative rates by taking into account solely the dipole-dipole interaction (see Eqs. (B.18') and (B.43') of Mathematical Appendices to Ref. [18]).

An analogous comparison for the non-radiative rates is shown in Figs. 5 and 6. Because the leading contribution to the non-radiative rates (10) is proportional to $\text{Im } \alpha$, and α reaches a maximum at the LSPR, the non-radiative decay is strongly enhanced when the emitter radiates at the plasmon-resonance frequency of the nanoparticle. Again all the approximate dipole-dipole interaction results, irrespective if obtained with α_R , α_C , $\alpha_{Mie;as}$, or α_{Mie} , together with the exact radiative rates obtained with a cut-off imposed at $l = 1$ coalesce to a single line. However, contrary to the radiative rates shown in Figs. 3 and 4, the non-radiative rates cannot be approximated by taking into account solely the dipole-dipole interaction. Clearly, as demonstrated by the exact non-radiative rates with the cut-offs imposed at $l = 2$, $l = 4$, and $l = 50$, respectively, the contribution of induced multipoles of the order $l \geq 2$ has a pronounced effect on the non-radiative rates. The latter shows up in the distance dependence of the non-radiative rate. This point is further elaborated in Sec. 4.2. Because the exact Γ_{nr} is always higher than the approximate one, whereas the exact and approximate Γ_r are essentially equal, the dipole-dipole approximation of Ref. [10] can only provide an upper bound on the apparent

quantum yield Y that is defined as the ratio $Y = \Gamma_r/(\Gamma_r + \Gamma_{nr})$. The different distance behavior of the radiative and non-radiative rates implies that the apparent quantum yield always vanishes at short distance, resulting in a quenching of the emission.

The results for the exact radiative and non-radiative rates shown in the figures were obtained using the freely available code CHEW [32] (see Appendix A for a brief description of the code). The exact rates comprise contributions of the induced multipoles with l up to $l_{max} = 50$. The exact radiative rates are derived from the total radiated power. The latter is calculated by the code CHEW by means of Eq. (108) of [6], where, in the notation of Ref. [6], the functions $f_{\gamma l}$ are given as linear combinations of spherical functions (Eqs. (69), (72) of [6]) taken at the dipole position, with the coordinate origin located at the sphere center. [In the special case of a dipole outside a homogeneous sphere, the coefficients $Q_{\gamma l}$ (Eq. (72) of [6]) that enter the definition of $f_{\gamma l}$ (Eq. (69) of [6]) reduce to the Mie's expansion coefficients (cf. Eqs. (32), (33) of [6]).] The exact power P_{abs} absorbed inside the particle is calculated by the code CHEW by means of Eq. (119) taken in combination with Eqs. (116) and (120) of [6]. In the special case of a dipole outside a homogeneous sphere one has, in the notation of Ref. [6], $N = n = 1$, and the coefficients $a_{\gamma l}$ and $b_{\gamma l}$ in the integrands of the respective integrals $I_{\gamma l}^{(s)}$ in Eq. (116) of [6] reduce to

$$a_{\gamma l} = 1/\mathcal{T}_{11;\gamma l}(2) = 1/T_{11;\gamma l}^+(1), \quad b_{\gamma l} = 0. \quad (17)$$

It is worth to emphasize that the exact rates shown in the figures were all calculated independently: (i) the fluorescence decay rates have been determined in CHEWFS from the imaginary part of a relevant dyadics (cf. Eq. (1) of Ref. [10] Eq. (135) of Ref. [6]), the radiative rates have been determined in CHEW from the total radiated power of a dipole escaping to infinity (Eqs. (108) and (124) of Ref. [6]), and the non-radiative rates have been determined in CHEW from the total Ohmic loss of dipole radiation (see Eqs. (111), (115), (116), (133) of Ref. [6]). One can verify that the sum of the radiative and non-radiative rates as obtained using CHEW coincides with the total decay rate as obtained using CHEWFS.

4 Discussion

4.1 A comparison with the Gersten and Nitzan rates

In the special case of a dipole outside a homogeneous sphere, the functional form of the respective exact expressions for the total radiated power [Eq. (108) of [6] with $f_{\gamma l} = j_l(kr_d) + \kappa_{\gamma l} h_l^{(1)}(kr_d)$, where $\kappa_{\gamma l}$ are the Mie's coefficients (a_l for $\gamma = M$ and b_l for $\gamma = E$; cf Eqs. (69), (32), and (34) of [6])] and for the power P_{abs} absorbed inside the particle [Eq. (119) of [6] with $d_{\gamma l} = h_l^{(1)}(kr_d)$] look quite similar. However, whereas in Eq. (108) of [6] the Hankel functions are with increasing l multiplied by rapidly decreasing Mie's coefficients, in Eq. (119) of [6] the Hankel functions are multiplied with increasing l by much slowly decreasing values of the integrals $I_{\gamma l}^{(s)}$ (Eqs. (116) of [6]) taken over the particle volume. The latter explains, which is also an intrinsic feature of the approximate

quasistatic Gersten and Nitzan theory [18], that in the small particle limit (i) $l = 1$ is enough to describe the radiative rates (see Eqs. (B.18') and (B.43') of Mathematical Appendices to Ref. [18]), whereas, in principle, (ii) an infinite series in l is required to describe the non-radiative rates (see Eqs. (B.24') and (B.45') of Mathematical Appendices to Ref. [18]). This is also the reason why the *non-radiative* rates calculated by the Gersten and Nitzan theory agree much better with the exact electrodynamic non-radiative rates as confirmed by Figs. 7 and 8. In arriving at the results, the same formulas as Eqs. (3) and (4) of Ref. [12] were used with the respective terms $|1 - \Delta|^2$, where $\Delta(\perp)$ and $\Delta(\parallel)$ are the Gersten and Nitzan image enhancement factors, being essentially equal to one. (In the present case, the ratios $\Delta/\Gamma_{r,int}$, with $\Gamma_{r,int}$ denoting the intrinsic vacuum radiative rate, are of the order of 10^{-10} .) That is analogous to Ref. [19], where $|1 - \Delta|^2 \approx 1$ is implicit upon comparing Eqs. (5) and (6) with the exact formulas (B.18') and (B.43') of Mathematical Appendices to Ref. [18]. The above conclusions, i.e. that the molecular dipole excites all the multipoles of the sphere, but only the dipole radiates, whereas higher-order multipole terms gives rise to dissipation, have been confirmed within the quasistatic approximation also by other researcher [34, 35, 36].

The Gersten and Nitzan results are supported by experiment [12]. A mismatch between the theoretical and the measured non-radiative rates reported in earlier work [4, 7] may partly be attributed to nonlocal effects [33] and, partly, to the fact that a point dipole may be a too crude approximation for fluorophores but remains rather good for phosphors (the latter have a dipole strength that is reduced by orders of magnitude compared to that of fluorophores [12]). The nonlocal effects, in general, lead to significantly *greater* fluorescence rates and *smaller* non-radiative decay rates for the admolecules [33]. Eventually, Sec. 4.4 below demonstrates that the theoretical values of non-radiative rates for fluorescence near a LSPR can be further decreased toward the measured non-radiative rates [4, 7] by accounting for size corrected dielectric function.

Although the approximate quasistatic Gersten and Nitzan theory [18] has been shown to be superior to the dipole-dipole approximation of Ref. [10], the use of the Gersten and Nitzan theory [18] is also not without limitations [19]. For instance, in contrast to the exact Chew expressions for the *radiative* rates [13, 14], the theory of Gersten and Nitzan [18] does not yield the correct asymptotic results for a flat surface in the limit $a \rightarrow \infty$ with a fixed value of the separation d of the dipole from the surface of a sphere. Moreover, as emphasized by Kim et al [19], in addition to the conditions $a \ll \lambda$ and $d \ll \lambda$, the value of sphere radius a cannot be too large for a fixed d if the Gersten and Nitzan model [18], and hence any dipole-dipole coupling model, is to be applied for the *radiative* rates. Eventually, contrary to the exact electrodynamic results, the ratios Γ_{nr}/Γ_0 and Γ_r/Γ_0 , depend on the intrinsic vacuum radiative rate, because both image enhancement factors $\Delta(\perp)$ and $\Delta(\parallel)$ of the Gersten and Nitzan model depend on $\Gamma_{r,int}$ [18].

4.2 The distance dependence of non-radiative rates

The approximate non-radiative rates (10) gave an impression that their short distance dependence is, like in the Förster energy transfer, characterized by a z^{-6} -like dependence.

However, it has been just shown (see Figs. 5 and 6) that a dipole-dipole coupling is not appropriate to describe the non-radiative rates of a dipole emitter in a proximity of a MNP. Taking for example $\Gamma_{nr;\parallel}$, the exact $\Gamma_{nr;\parallel}$ for the emission wavelength of 612 nm shown in Fig. 5 is at the distances of 5 nm, 10 nm, and 15 nm from the AgNP surface by 101%, 33%, and 17% higher than the approximate dipole-dipole contribution of Ref. [10]. Similarly, the exact $\Gamma_{nr;\parallel}$ for the emission wavelength of 354 nm shown in Fig. 6 is at the distances of 5 nm, 10 nm, and 15 nm from the AgNP surface by 56%, 20%, and 11% higher than the approximate dipole-dipole contribution of Ref. [10]. Because of the importance of the higher-order ($l > 1$) multipoles contribution, which decay as $z^{-(2l+4)}$, it makes rather sense to consider the dependence of the non-radiative rates on the separation d of the dipole from the surface of a sphere [34, 37]. Depending on the particle radius, the non-radiative rates can decay between $\approx d^{-5}$ and d^{-3} , wherein a near d^{-3} decay is already observed for the particle radii $\gtrsim 10$ nm (see Figs. 16 and 17 in Sec. 3.6 of Ref. [34] and Fig. 2.15 of Ref. [37]). A slower than d^{-6} dependence of the non-radiative rates is valid even for particles as small as 1 nm in diameter [37]. Upon taking into account the results by Dulkeith [37], one can conclude that even for MNPs with the radius as small as 0.5 nm and the emitter as far as the distance of $3a$ from the particle surface, the emitter and the MNP do not interact exclusively through dipole-dipole coupling.

A full quantum-mechanical calculation for a *spherical* metal surface obtained within the time-dependent local density approximation (TDLDA) by Ekardt and Penzar [38] essentially confirms the above picture. Formally similar to the classical electrodynamic case [1, 6], the quantum-mechanical non-radiative rates (see Eq. (5) in Ref. [38]) were given as an infinite series over l of the terms proportional to $(\text{Im } \alpha_l)/z^{2l+4}$, where α_l is the l -pole polarizability of the sphere. The difference with the classical case is in that $\alpha_l(\omega)$ is the quantum-mechanical *dynamical* l -pole polarizability calculated within the TDLDA. Because each term in the series has a different distance dependence, the overall distance dependence of the non-radiative rates cannot be uniquely determined, simply because everything is mixed up [38]. Note in passing that the TDLDA results incorporate the so-called nonlocal dielectric response [33, 39, 40] without any approximation.

Unfortunately, a detailed comparison of the classical electrodynamic results [1, 6] against the full quantum-mechanical calculation remains to be an open question. An obstacle in comparing quantum-mechanical TDLDA with the classical electrodynamic is that the former works with an electron density parameter [38], from which there is still some distance to calculate the dielectric function of say silver, which would then serve as the input parameter for the classical electrodynamic calculations. Thus at present it is not possible to answer conclusively at which distances from a MNP surface the classical results can no longer be applied.

4.3 The power P_{abs} absorbed inside the particle

It turns out that it is more reliable to calculate the power P_{abs} absorbed inside the particle by using the formula (13). On the other hand, a direct integration approach of Carminati et al [10] leads to a contradiction. Indeed, according to the definition of the polarizability,

the field inside the particle, \mathbf{E}_{in} , is related to the external field \mathbf{E}_{exc} acting on the particle as follows:

$$\mathbf{E}_{in} = \frac{3\alpha}{4\pi a^3(\varepsilon - 1)} \mathbf{E}_{exc}. \quad (18)$$

On using the parametrization (6) of the polarizability,

$$\mathbf{E}_{in} = \frac{3}{(\varepsilon + 2)} \frac{\mathbf{E}_{exc}}{\left(1 - A_2 \frac{k^2}{4\pi a} \alpha_R - iA_3 \frac{k^3}{6\pi} \alpha_R\right)}. \quad (19)$$

When this expression is substituted into the formula (B.1) of Ref. [10],

$$P_{abs} = \frac{4}{3} \pi a^3 \frac{\omega \varepsilon_0}{2} \varepsilon'' |\mathbf{E}_{in}|^2, \quad (20)$$

one arrives at

$$P_{abs} = 4\pi a^3 \frac{\omega \varepsilon_0}{2} \frac{3 \varepsilon''}{|\varepsilon + 2|^2} \frac{|\mathbf{E}_{exc}|^2}{\left|1 - A_2 \frac{k^2}{4\pi a} \alpha_R - iA_3 \frac{k^3}{6\pi} \alpha_R\right|^2}. \quad (21)$$

With the help of the identity (B.3) of Ref. [10],

$$4\pi a^3 \frac{3 \varepsilon''}{|\varepsilon + 2|^2} = 4\pi a^3 \operatorname{Im} \left(\frac{\varepsilon - 1}{\varepsilon + 2} \right) = \operatorname{Im} \alpha_R, \quad (22)$$

and upon comparing with (cf. Eq. (B.5) of Ref. [10])

$$\operatorname{Im} \alpha = \frac{(\operatorname{Im} \alpha_R)}{\left|1 - A_2 \frac{k^2}{4\pi a} \alpha_R - iA_3 \frac{k^3}{6\pi} \alpha_R\right|^2} + \left[(\operatorname{Im} A_2) \frac{k^2}{4\pi a} + A_3 \frac{k^3}{6\pi} \right] |\alpha|^2, \quad (23)$$

that follows from the parametrization (6), one eventually arrives at

$$P_{abs} = \frac{\omega \varepsilon_0}{2} \left\{ \operatorname{Im} \alpha - \left[(\operatorname{Im} A_2) \frac{k^2}{4\pi a} + A_3 \frac{k^3}{6\pi} \right] |\alpha|^2 \right\} |\mathbf{E}_{exc}|^2. \quad (24)$$

Actually $\operatorname{Im} A_2 \neq 0$ only for $\alpha_{Mie;as}$, in which case

$$\operatorname{Im} A_2 = \frac{3}{5} \frac{\varepsilon''}{|\varepsilon - 1|^2}, \quad (25)$$

whereas $\operatorname{Im} A_2 \equiv 0$ for α_R , α_C , and α_{MW} . Upon comparing the two expressions (12) and (24) for the absorbed power P_{abs} one finds that, in the case of $\alpha_{Mie;as}$, they differ in the term proportional to $\operatorname{Im} A_2$. The result (24) would imply a modification of the non-radiative and radiative rate formulae of Ref. [10]. However, the latter difference of the two expressions for P_{abs} appears to be a consequence of that Eq. (20) is only an approximation to

$$P_{abs} = \frac{\omega \varepsilon_0}{2} \varepsilon'' \int_V |\mathbf{E}_{in}|^2 dV, \quad (26)$$

where the integral is over the volume of the particle. Eqs. (12) and (26) are equivalent. However, the hypothesis that, for a given constant homogeneous external field, the internal field inside the particle is a constant, and which leads to Eq. (20), introduces an order x^2 deviation from the exact result. Although at a first approximation the internal field inside the particle can indeed be assumed to be a constant, this is of course not true exactly [41]. It has been shown that the very form of the dynamic depolarization term in $\alpha_{Mie;as}$ implicitly implies an order x^2 deviations from the constant internal field [31]. The order x^2 deviation from the exact result for P_{abs} when using Eq. (20) is of the same order as the $\text{Im } A_2$ term that makes the difference between Eqs. (12) and (24). It is therefore natural to assume that if the volume integration in Eq. (26) were performed by taking into account the order x^2 deviation from the constant internal field, one would arrive at the result (12) obtained directly from the absorption cross section.

4.4 Effect of size corrections to the bulk dielectric function

It is generally accepted that for radii of MNPs smaller than the mean free path of conduction electrons (42 nm for Au and 52 nm for Ag) the dielectric function of free electron metals should be corrected due to a reduced mean-free path of the electrons because of the scattering of the electrons on the MNP surface [24]

$$\varepsilon_s(\omega) = \varepsilon_b(\omega) - \varepsilon_b^D(\omega) + \varepsilon_{sd}^D(\omega). \quad (27)$$

Here, ε_b is the bulk metal dielectric function, and ε_b^D is the Drude dielectric function

$$\varepsilon_b^D(\omega) = 1 - \omega_p^2 / [\omega(\omega + i\gamma)], \quad (28)$$

describing the bulk metal conduction electrons with the plasma frequency ω_p and the bulk damping constant γ . The term ε_{sd}^D differs from ε_b^D in that γ is replaced by the size-corrected value [24, 26]

$$\gamma_{sd} = \gamma + Av_F/a, \quad (29)$$

where v_F is the Fermi velocity and A (not to be confused with A'_j s in the preceding sections) is a phenomenological fitting parameter [24]. For gold and silver the size-correction becomes appreciable when, as in the present case, the sphere radius is $\lesssim 8$ nm (see for instance Fig. 4 [25]), i.e. less than one fifth of the mean free path of conduction electrons. The following parameters were employed for silver: $v_F = 1.39$ nm fs⁻¹, $\omega_p = 72700$ cm⁻¹, and $\gamma = 145$ cm⁻¹ [42, 43]. Given the above parameters, $\varepsilon(354 \text{ nm}) = -2.03 + 0.6i$ would change into $\varepsilon(354 \text{ nm}) \approx -2.028 + 0.686i$ for $A = 0.25$ and into $\varepsilon(354 \text{ nm}) \approx -2.008 + 0.945i$ for $A = 1$. Similarly, $\varepsilon(612 \text{ nm}) = -15.04 + 1.02i$ would change into $\varepsilon(612 \text{ nm}) = -15.022 + 1.466i$ for $A = 0.25$ and into $\varepsilon(612 \text{ nm}) = -14.849 + 2.789i$ for $A = 1$. Following experimental results for individual gold NPs down to $a = 2.5$ nm by Berciaud et al [25], the value of $A = 0.25$ could be employed on the grounds of the similarity in the band structure of silver and gold [25]. Depending on the sample preparation, the value of $A = 1$ may be suitable in other cases [24].

As shown in Figs. 7 and 8 by a dash-dot line, the effect of the size corrected dielectric function on the non-radiative rates is rather pronounced for $A = 1$. At the wavelength of 354 nm, the size correction has the effect of decreasing the non-radiative rates, whereas for the wavelength of 612 nm the size correction has the opposite effect. Although the above results may at a first glance appear counterintuitive, they can be explained rather straightforwardly. Take for instance the leading $l = 1$ contribution, which is well approximated by Eqs. (10). Eqs. (10) show that the leading $l = 1$ contribution to the non-radiative decay is controlled through $\text{Im } \alpha$ rather than ε'' . According to Eq. (22), $\text{Im } \alpha_R$ depends on ε'' as $3/(\varepsilon'')^2$ near the dipolar LSPR. Therefore, at the proximity of the LSPR, increasing ε'' results in *smaller* values of $\text{Im } \alpha_R$ that causes the non-radiative decay to *decrease*. Thus by properly accounting for the size corrected dielectric function at the proximity of the LSPR may yield an additional mechanism for decreasing the theoretical values of non-radiative rates toward the measured non-radiative rates [4, 7].

On the other hand, ε' is typically ten times larger in magnitude than ε'' far away from the LSPR. Consequently a change in ε'' has only a minor effect on the denominator Eq. (22) and $\text{Im } \alpha_R$ becomes essentially proportional to $3\varepsilon''$. Thus far away from the LSPR increasing ε'' results in *larger* value of $\text{Im } \alpha_R$ that causes the non-radiative decay to *increase*.

5 Conclusions

The methods based on dipole-dipole coupling [10, 18] have known limitations in describing the radiative rates [19]. In line with earlier quasistatic results [18, 34, 35, 36], the present work reaffirms that the dipole-dipole coupling severely underestimate the non-radiative rates even in the parameter range, where it rather satisfactorily describes the radiative rates. An approximate analytical dipole-dipole coupling approach, such as that of Ref. [10], may fail without any warning even for relatively small particles. The dipole-dipole interaction results of Carminati et al [10] cannot be improved by any generalization of their expression for the dipolar polarizability, either by supplying the dynamic depolarization term or by taking the full Mie's expression. To correctly describe the radiative and non-radiative decay of fluorophores, chromophores, and quantum dots close to a metallic nanoparticle, the use of a complete theory is recommended [1, 6, 8, 13, 14, 15]. Taking a Ag spherical nanoparticle (AgNP) with the radius of 5 nm as an example, a significant contribution (between 50% and 101% of the total value) of the higher-order ($l > 1$) multipoles to the non-radiative rates was found at the emitter distance of 5 nm from the AgNP surface. Consequently, a dipole-dipole approximation can yield only an upper bound on the apparent quantum yield. In general, the higher-order ($l > 1$) multipole contributions to the non-radiative rates cannot be neglected, even if a particle has a radius as small as $a = 0.5$ nm and the dipole emitter is further than 15 nm from the particle surface. The effect of the higher-order multipole contributions shows up in a markedly slower than d^{-6} distance dependence of the non-radiative rates. The non-radiative rates calculated with the approximate quasistatic Gersten and Nitzan method, which takes into

account the contribution of higher-order ($l > 1$) multipoles, were found to be in much better agreement with exact electrodynamic results. Finally, the size corrected metal dielectric function was shown to decrease the non-radiative rates near the dipolar surface plasmon resonance.

6 Acknowledgments

I thank G.-Y. Guo and R. Hammerling for a careful reading of the manuscript and useful suggestions.

A A brief description of the codes CHEW and CHEWFS with instructions how to adapt them to case of a homogeneous sphere

The Fortran F77 codes CHEWFS [17] and CHEW [32], which have been written according to the theory developed in Refs. [6, 8] and which have been free available since October 2004, are designed to calculate various decay rates of a dipole emitter interacting with a multi-coated sphere with an arbitrary number of shells. The emitter can be located either inside or outside a sphere.

CHEWFS [17] calculates the total decay rate and frequency shift directly from the respective imaginary and real parts of the Green's function at coinciding arguments (cf. Eqs. (135) and (137) of Ref. [6]). CHEWFS returns files *dpfshifftm.dat* (containing frequency shifts) and *dipqmratesm.dat* (containing total decay rates).

CHEW [32] calculates the radiative and non-radiative rates, which are both calculated classically. The radiative rate is determined from the total radiated power of a dipole escaping to infinity. The latter is found by integrating the radial component of the time-averaged Poynting vector over the surface of a sphere with a radius going to infinity (cf. Eq. (88) of Ref. [6]). The output is in files *dipratesm.dat* and *dipratesv.dat*. The non-radiative rates are determined by CHEW from the Ohmic losses inside absorptive shells (cf. Eqs. (110) and (111) of Ref. [6]). The output is in files *dipnrratesm.dat* and *dipnrratesv.dat*, which contains non-radiative rates normalized to the radiative rates in a corresponding infinite space.

The output files **m.dat* and **v.dat* differ only in that the rates are normalized with respect to those in the local medium at the dye position and in vacuum respectively. Each output file has data organized in four columns: normalized radial position (in the units of the bead radius) and the corresponding quantities for the respective tangential, radial, and averaged dipole orientations (from left to right). [The fourth column is not a simple average of the second and third columns but is calculated according to Eq. (123) of Ref. [6] as $(\Gamma_{\perp} + 2\Gamma_{\parallel})/3$]. To modify the default versions of the two codes to the present case of a homogeneous sphere, the following steps have to be performed:

- The layers of a coated sphere with N shells are counted from one for the sphere core up to $LCS=N+1$ for the outermost shell and $N+2$ for the host medium. See also Fig. 1 of [6]. A homogeneous sphere has no shell and thus $N=0$. Consequently, the value of the integer parameter LCS , which controls the number of coatings, has to be set to $LCS=1$. Next the integer parameter $ILCS$ has to be set to $ILCS=1$. The latter ensures that the dielectric constant specified by the complex parameter $CCEPS$ becomes the dielectric constant of the sphere (core).
- The value of the complex parameter $CCEPS$ has to become one of the two values of the complex dielectric constant. At the same time the value of the integer parameter $NMAT=0$ has to be adopted. The latter choice corresponds to a dispersionless medium and should also be imposed if the data specified by $CCEPS$ is given preference. Otherwise, for $NMAT \geq 1$, the resulting value of the dielectric constant, which enters the Mie coefficients as the complex variable $ZEPS1$, is overwritten by either the Drude data or the real material data.
- The integer parameter $NABS$, which specifies the total number of absorbing layers, and $IABS$, which carries the number of the absorbing layer, have to be both set to one.
- The value of the real parameter NX specifies in the units of the sphere radius the length of the radial interval on which the decay rates are calculated. The value of NX is used to control the “do 200 il=1,nx” loop.
- The angular momentum number l of the induced multipoles involved in the calculation is controlled through the value of the variable LMX . The data setting $LMX/1/$ then forces the code to take into account only the dipolar contribution. The arrays of the codes are dimensioned with the integer parameter $LMAX$, where at present $LMAX=60$. The variable LMX can take any value between 1 and $LMAX$.

B Supporting Information Available

A MS Windows executable [44] is provided which calculates all the approximate rates shown here.

References

- [1] R. Ruppin, "Decay of an excited molecule near a small metal sphere," *J. Chem. Phys.* 76 (1982) 1681-1684.
- [2] B. Dubertret, M. Calame, A.J. Libchaber, "Single-mismatch detection using gold-quenched fluorescent oligonucleotides," *Nat. Biotechnol.* 19 (2001) 365-370.
- [3] J.R. Lakowicz, "Radiative decay engineering: Biophysical and biomedical applications," *Anal. Biochem.* 298 (2001) 1-24.
- [4] E. Dulkeith, A.C. Morteani, T. Niedereichholz, T.A. Klar, J. Feldmann, S.A. Levi, F.C.J.M. van Veggel, D.N. Reinhoudt, M. Möller, D.I. Gittins, "Fluorescence quenching of dye molecules near gold nanoparticles: Radiative and nonradiative effects," *Phys. Rev. Lett.* 89 (2002) 203002.
- [5] J.R. Lakowicz, "Radiative decay engineering 5: metal-enhanced fluorescence and plasmon emission," *Anal. Biochem.* 337 (2005) 171-194.
- [6] A. Moroz, "A recursive transfer-matrix solution for a dipole radiating inside and outside a stratified sphere," *Ann. Phys. (NY)* 315 (2005) 352-418.
- [7] E. Dulkeith, M. Ringler, T.A. Klar, J. Feldmann, A. Muñoz Javier, W.J. Parak, "Gold nanoparticles quench fluorescence by phase induced radiative rate suppression," *Nano Lett.* 5 (2005) 585-589.
- [8] A. Moroz, "Spectroscopic properties of a two-level atom interacting with a complex spherical nanoshell," *Chem. Phys.* 117 (2005) 1-15.
- [9] T.L. Jennings, J.C. Schlatterer, M.P. Singh, N.L. Greenbaum, G.F. Strouse, "NSET molecular beacon analysis of hammerhead RNA substrate binding and catalysis," *Nano Lett.* 6 (2006) 1318-1324.
- [10] R. Carminati, J.-J. Greffet, C. Henkel, J.M. Vigoureux, "Radiative and non-radiative decay of a single molecule close to a metallic nanoparticle," *Opt. Commun.* 261 (2006) 368-375.
- [11] P. Anger, P. Bharadwaj, L. Novotny, "Enhancement and quenching of single-molecule fluorescence," *Phys. Rev. Lett.* 96 (2006) 113002.
- [12] T. Soller, M. Ringler, M. Wunderlich, T.A. Klar, J. Feldmann, H.-P. Josel, Y. Markert, A. Nichtl, K. Kürzinger, "Radiative and nonradiative rates of phosphors attached to gold nanoparticles," *Nano Lett.* 7 (2007) 1941-1946.
- [13] H. Chew, "Transition rates of atoms near spherical surfaces," *J. Chem. Phys.* 87 (1987) 1355-1360.

- [14] H. Chew, "Radiation and lifetimes of atoms inside dielectric particles," *Phys. Rev. A* 38 (1988) 3410-3416.
- [15] Y.S. Kim, P.T. Leung, T.F. George, "Classical decay rates for molecules in the presence of a spherical surface: A complete treatment," *Surf. Sci.* 195 (1988) 1-14.
- [16] E.W. Palik (Ed.), *Handbook of Optical Constants of Solids*, Academic Press, San Diego, 1985.
- [17] The source code for CHEWFS can be downloaded from <http://www.wave-scattering.com/chewfs.f>
- [18] J. Gersten, A. Nitzan, "Spectroscopic properties of molecules interacting with small dielectric particles," *J. Chem. Phys.* 75 (1981) 1139-1152.
- [19] Y.S. Kim, P.T. Leung, T.F. George, "Radiative decay rates for molecules near a dielectric sphere," *J. Phys. Chem.* 92 (1988) 6206-6208.
- [20] T. Pons, I.L. Medintz, K.E. Sapsford, S. Higashiya, A.F. Grimes, D.S. English, H. Mattoussi, "On the quenching of semiconductor quantum dot photoluminescence by proximal gold nanoparticles," *Nano Lett.* 7 (2007) 3157-3164.
- [21] S. Palomba, R.E. Palmer, "Optical coupling of core-shell quantum dots to size-selected gold clusters," *J. Appl. Phys.* 104 (2008) 094316.
- [22] N. Nerambourg, R. Praho, M.H.V. Werts, D. Thomas, M. Blanchard-Desce, "Hydrophilic monolayer-protected gold nanoparticles and their functionalisation with fluorescent chromophores," *Int. J. Nanotechnol.* 5 (2008) 722-740.
- [23] M. Kondon, J. Kim, N. Udawatte, D. Lee, "Origin of size-dependent energy transfer from photoexcited CdSe quantum dots to gold nanoparticles," *J. Phys. Chem. C* 112 (2008) 6695-6699.
- [24] U. Kreibig, C.V. Fragstein, "The limitation of electron mean free path in small silver particles," *Z. Phys. A* 224 (1969) 307-323.
- [25] S. Berciaud, L. Cognet, P. Tamarat, B. Lounis, "Observation of intrinsic size effects in the optical response of individual gold nanoparticles," *Nano Lett.* 5 (2005) 515-518.
- [26] A. Moroz, "Electron mean-free path in a spherical shell geometry," *J. Phys. Chem. C* 112 (2008) 10641-10652.
- [27] A. Wokaun, J.P. Gordon, P.F. Liao, "Radiation damping in surface-enhanced Raman scattering," *Phys. Rev. Lett.* 48 (1982) 957-960.
- [28] M. Meier, A. Wokaun, "Enhanced fields on large metal particles: dynamic depolarization," *Opt. Lett.* 8 (1983) 581-583.

- [29] J.D. Jackson, *Classical Electrodynamics*, 3rd ed, John Wiley & Sons, New York, 1999.
- [30] C.F. Bohren, D.R. Huffman, *Absorption and Scattering of Light by Small Particles*, John Wiley & Sons, New York, 1998.
- [31] A. Moroz, “Depolarization field of spheroidal particles,” *J. Opt. Soc. Am. B* 26 (2009) 517-527.
- [32] The source code for CHEW can be downloaded from <http://www.wave-scattering.com/chew.f>.
- [33] J. Vielma, P. T. Leung, “Nonlocal optical effects on the fluorescence and decay rates for admolecules at a metallic nanoparticle,” *J. Chem. Phys.* 126 (2007) 194704.
- [34] G. W. Ford and W. H. Weber, “Electromagnetic interactions of molecules with metal surfaces,” *Phys. Rep.* 113 (1984) 195-287.
- [35] H. Metiu, *Prog. Surf. Sci.* 17 (1984) 153-320.
- [36] P. Bharadwaj and L. Novotny, *Opt. Express* 15 (2007) 14266-14274.
- [37] E. Dulkeith, PhD Thesis: “Optische Charakterisierung von Hybridsystemen aus Gold Nanopartikeln und Farbstoffmolekülen,” p. 35, Fig. 2.15. Available at http://edoc.ub.uni-muenchen.de/2789/1/Dulkeith_Eric.pdf.
- [38] W. Ekardt, Z. Penzar, “Nonradiative lifetime of excited states near a small metal particle,” *Phys. Rev. B* 34 (1986) 8444-8448.
- [39] G. S. Agarwal, S. V. O’Neil, “Effect of hydrodynamic dispersion of the metal on surface plasmons and surface-enhanced phenomena in spherical geometries,” *Phys. Rev. B* 28 (1983) 487493.
- [40] P. T. Leung, “Decay of molecules at spherical surfaces: Nonlocal effects,” *Phys. Rev. B* 42 (1990) 7622-7625.
- [41] A.F. Stevenson, “Electromagnetic scattering by an ellipsoid in the third approximation,” *J. Appl. Phys.* 24 (1953) 1143-1151.
- [42] M.A. Ordal, R.J. Bell, R.W. Alexander, Jr., L.L. Long, M.R. Querry, “Optical properties of fourteen metals in the infrared and far infrared: Al, Co, Cu, Au, Fe, Pb, Mo, Ni, Pd, Pt, Ag, Ti, V, and W,” *Appl. Opt.* 24 (1985) 4493-4499.
- [43] See a compilation of Drude fit parameters of various metals at <http://www.wave-scattering.com/drudefit.html>.
- [44] The MS Windows executable can be downloaded from <http://www.wave-scattering.com/crmnt.exe>.

Figure captions

Figure 1 - Normalized fluorescence decay rates versus the distance z to the center of a AgNP of radius $a = 5$ nm for the emission wavelength $\lambda = 612$ nm. The exact rates shown by a solid black line here and in other figures of the paper comprise the contribution of the induced multipoles with l up to $l_{max} = 50$. The exact rates with an imposed cut-off at $l = 1$ are shown by a dash (red) line. The approximate dipole-dipole interaction results, irrespective if obtained with α_C (dash-dot line; blue), $\alpha_{Mie;as}$ (dot line line; green), or α_{Mie} (dash-dot-dot line; cyan), merge to a single line with that for the exact rates with a cut-off imposed at $l = 1$.

Figure 2 - The same as in Fig. 1 but for the emission wavelength $\lambda = 354$ nm.

Figure 3 - Normalized radiative rates versus the distance z to the center of a AgNP of radius $a = 5$ nm for the emission wavelength $\lambda = 612$ nm. The approximate dipole-dipole interaction results, irrespective if obtained with α_R (short dash line; mangenta), α_C (dash-dot line; blue), $\alpha_{Mie;as}$ (dot line line; green), or α_{Mie} (dash-dot-dot line; cyan), merge to a single line with that for the exact radiative rates. There is essentially no difference if, in the latter case, the cut-off is imposed at either $l = 1$ (dash line; red) or $l = 50$ (solid line; black).

Figure 4 - The same as in Fig. 3 but for the emission wavelength $\lambda = 354$ nm.

Figure 5 - Normalized non-radiative rates versus the distance z to the center of a AgNP of radius $a = 5$ nm for the emission wavelength $\lambda = 612$ nm. The approximate dipole-dipole interaction results, irrespective if obtained with α_R (short dash line; mangenta), α_C (dash-dot line; blue), $\alpha_{Mie;as}$ (dot line; green), or α_{Mie} (dash-dot-dot line; cyan), merge to a single line with that for the exact radiative rates with a cut-off imposed at $l = 1$ (dash line; red). The figure demonstrates a clear difference between the approximate non-radiative rates and exact non-radiative rates with a cut-off imposed at $l = 2$ (short dot line; purple), $l = 4$ (short dash-dot line; dark cyan), and $l = 50$ (solid line; black), respectively.

Figure 6 - Normalized non-radiative rates versus the distance z to the center of a AgNP of radius $a = 5$ nm for the emission wavelength $\lambda = 354$ nm. The exact rates with an imposed cut-off at $l = 1$ are shown by a dash (red) line.

Figure 7 - Comparison of the normalized Gersten and Nitzan non-radiative rates against the exact rates for a AgNP of radius $a = 5$ nm for the emission wavelength $\lambda = 612$ nm. The exact results with a size corrected dielectric function of silver for $A = 1$ are shown by dash-dot line (olive). All the rates were calculated with a cut-off $l_{max} = 50$.

Figure 8 - Comparison of the normalized Gersten and Nitzan non-radiative rates against the exact rates for a AgNP of radius $a = 5$ nm for the emission wavelength $\lambda = 354$ nm.

The exact results with a size corrected dielectric function of silver for $A = 1$ are shown by dash-dot line (olive). All the rates were calculated with a cut-off $l_{max} = 50$.

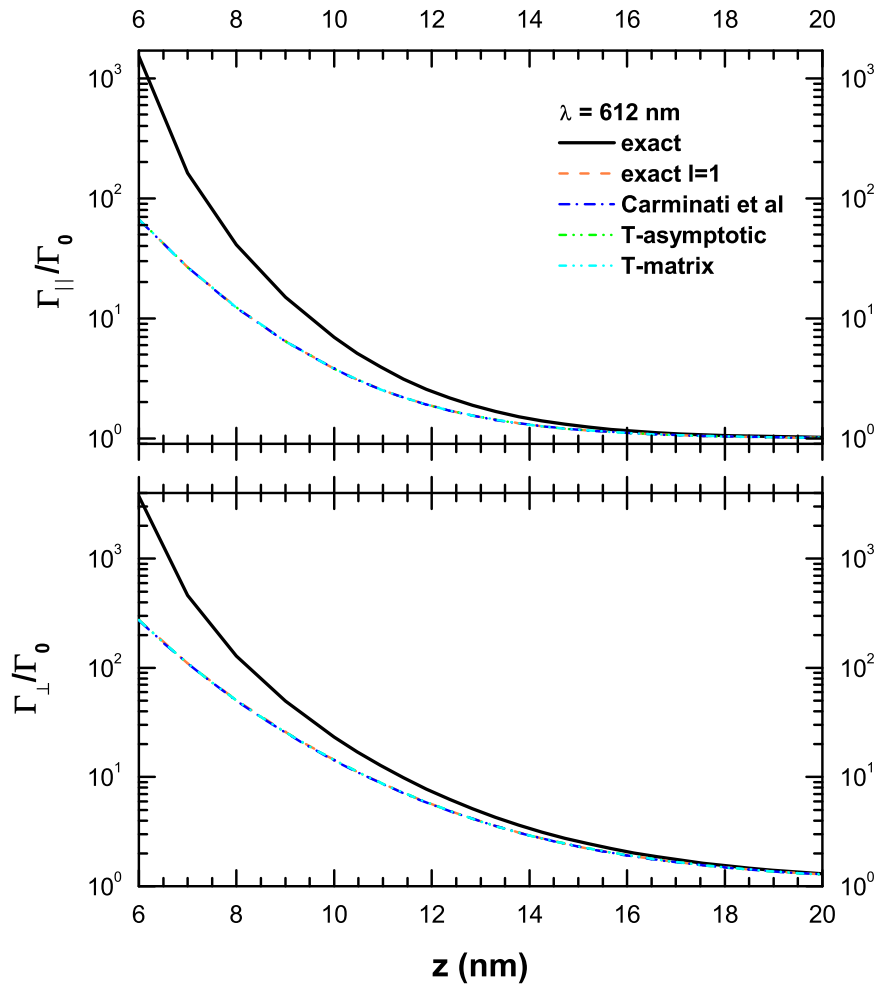


Figure 1:

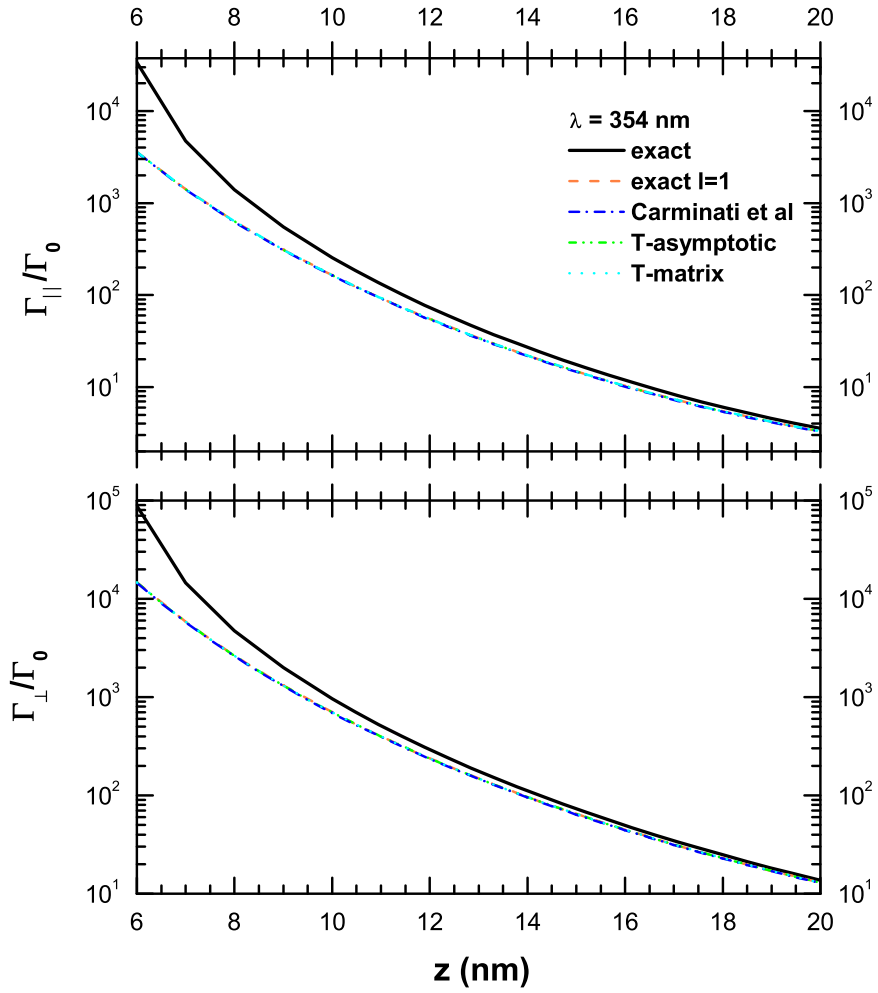


Figure 2:

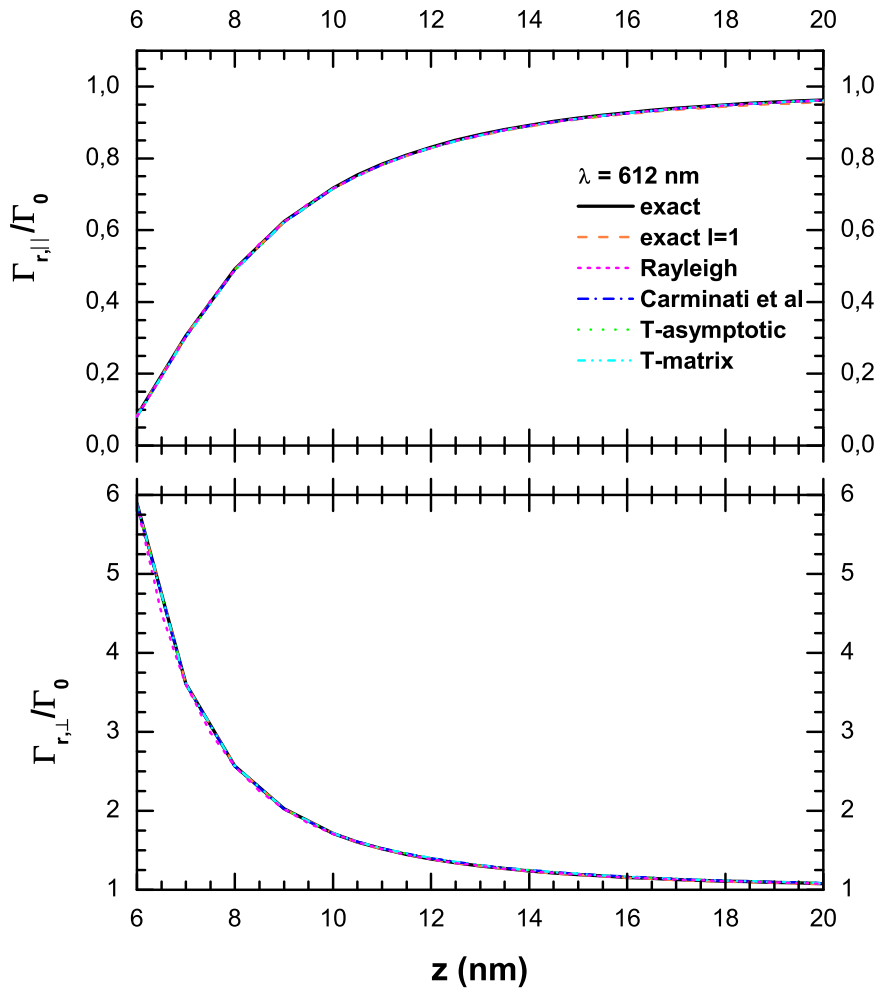


Figure 3:

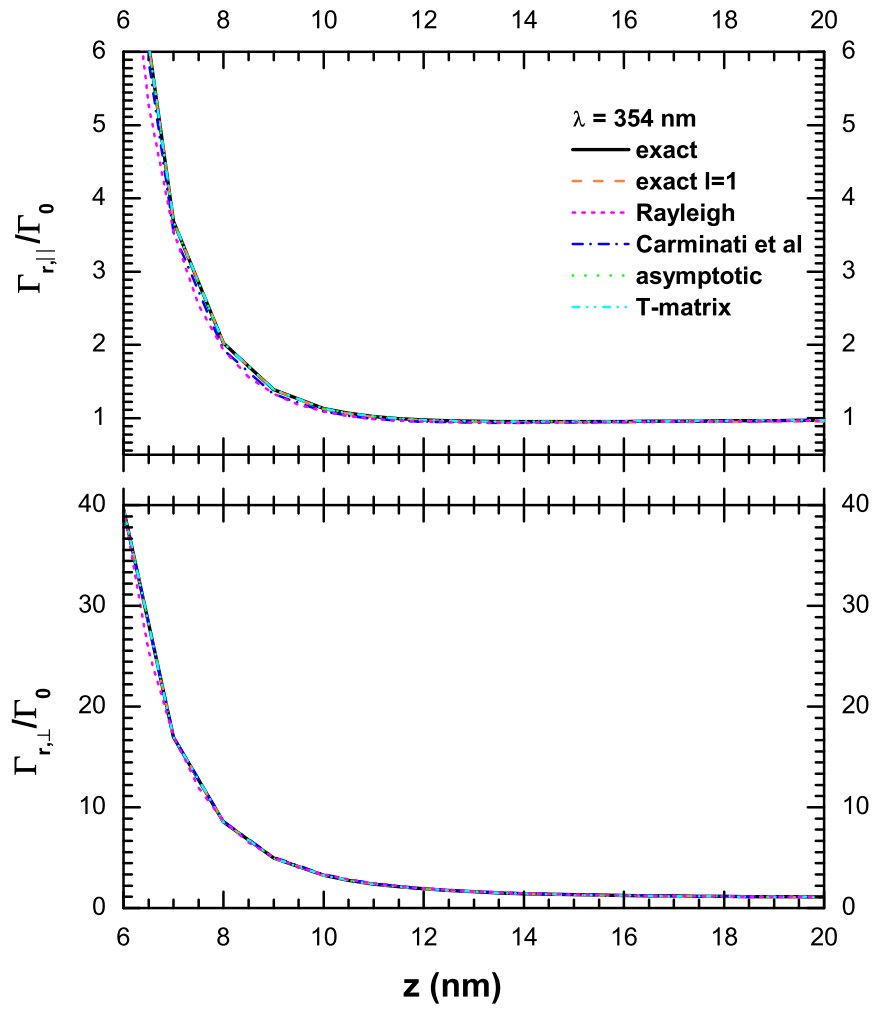


Figure 4:

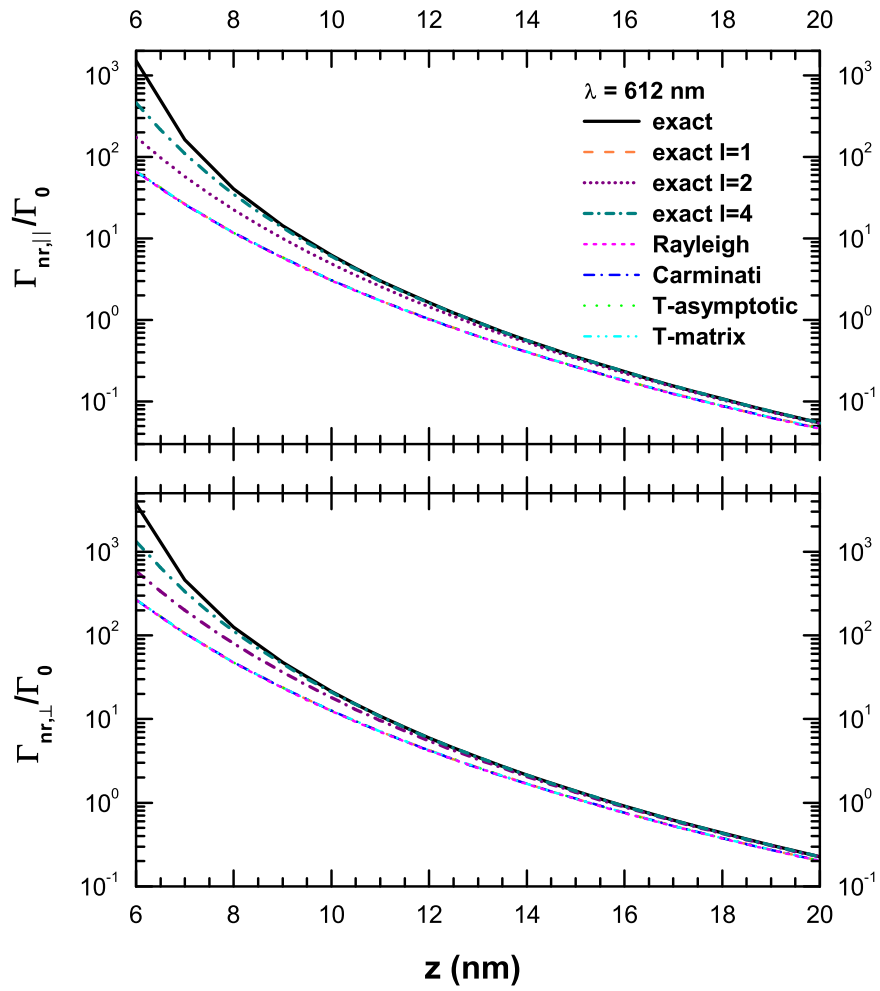


Figure 5:

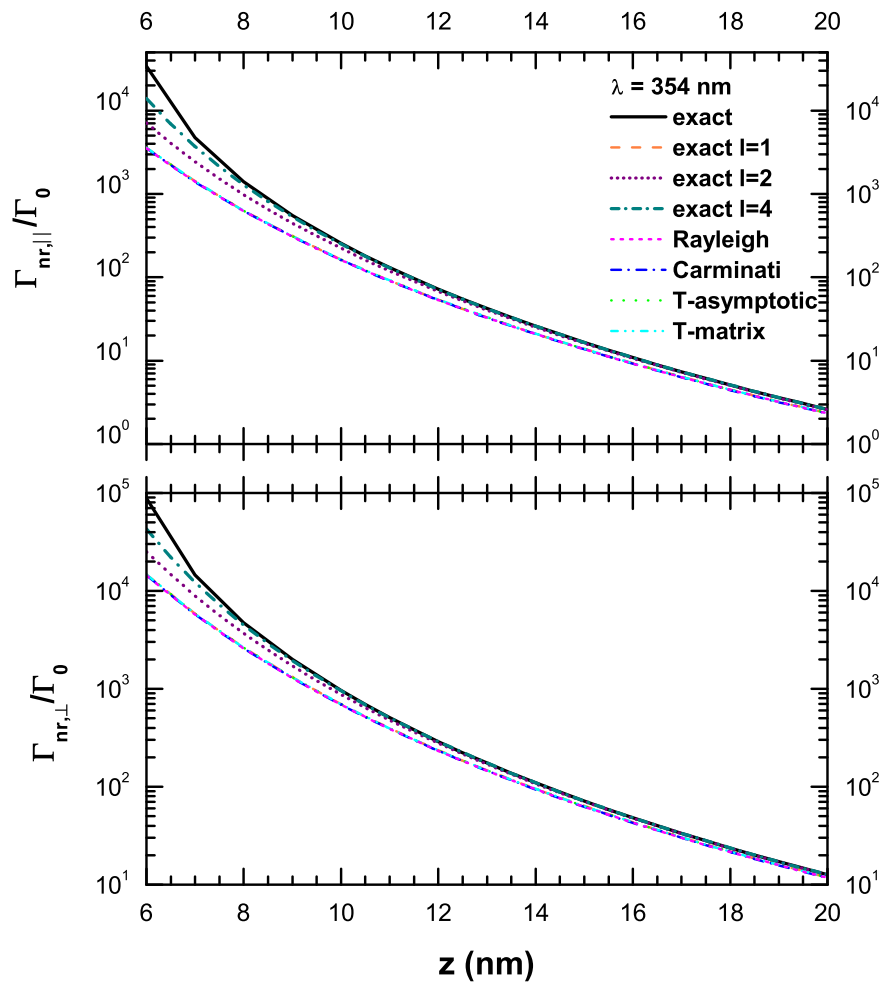


Figure 6:

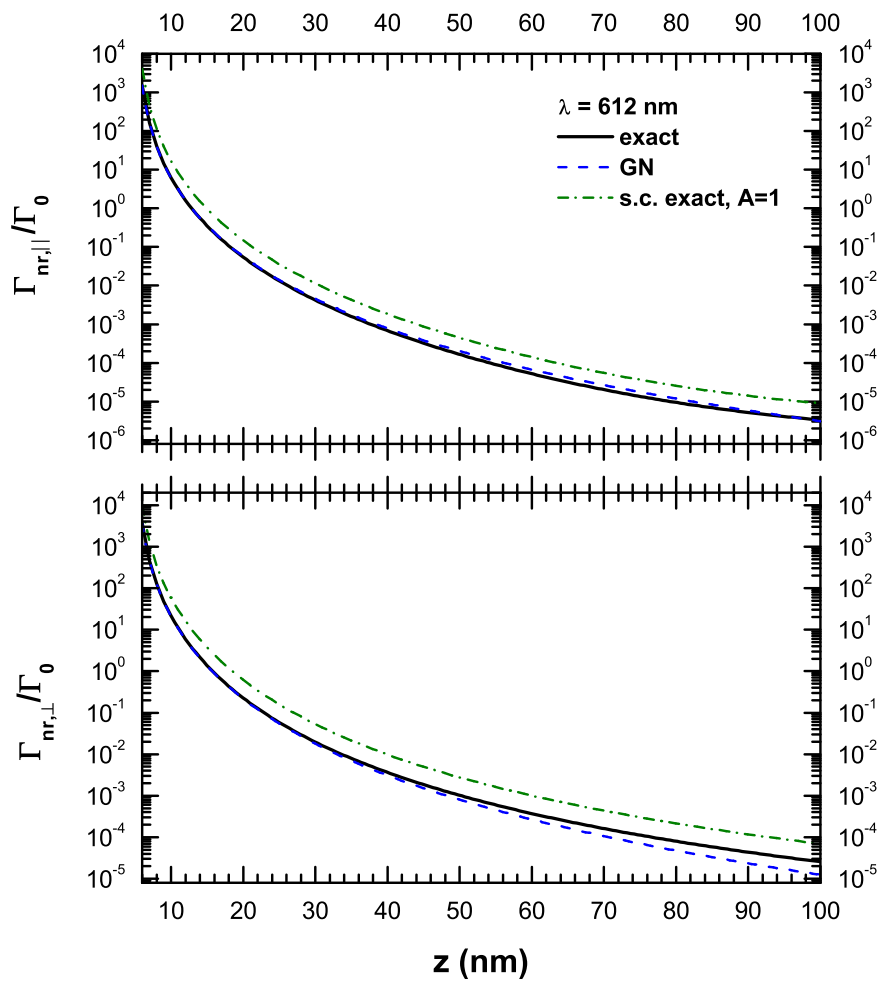


Figure 7:

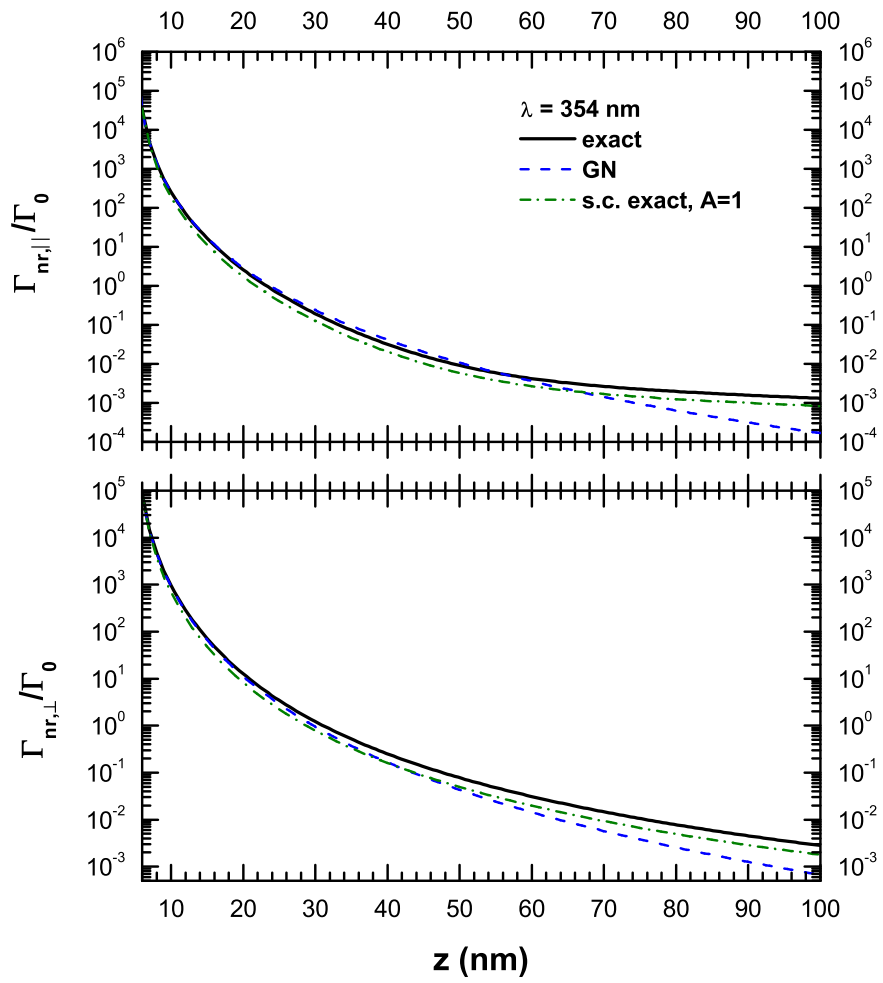


Figure 8: